https://doi.org/10.5194/egusphere-2022-1405
Preprint. Discussion started: 10 January 2023

Calibrating Radar Wind Profiler Reflectivity Factor using Surface Disdrometer Observations

Christopher R. Williams[1], Joshua Barrio[1], Paul E. Johnston[2], Paytsar Muradyan[3], and Scott E. Giangrande[4]

[1]Smead Aerospace Engineering Sciences Department, University of Colorado, Boulder, 80303, USA
[2]Cooperative Institute for Research in Environmental Sciences, University of Colorado, Boulder, 80316, USA
[3]Argonne National Laboratory, Lemont, Illinois, 60439, USA
[4]Environmental and Climate Sciences Department, Brookhaven National Laboratory, Upton, NY, 11793, US

Correspondence to: Christopher R. Williams (Christopher.Williams@colorado.edu)

Abstract. This study uses surface disdrometer reflectivity factor estimates to calibrate the vertical and off-vertical pointing radar beams produced by an Ultra High Frequency (UHF) band radar wind profiler (RWP) deployed at the US Department of Energy (DOE) Atmospheric Radiation Measurement (ARM) program Southern Great Plains (SGP) Central Facility in northern Oklahoma from April 2011 through July 2019. The methodology consists of five steps. First, the recorded Doppler velocity power spectra are adjusted to account for Nyquist velocity aliasing and coherent integration filtering effects. Second, the spectrum moments are calculated. The third step increases the signal-to-noise ratio (SNR) due to signal power leakage during the Fast Fourier Transform (FFT) calculation, which can exceed 20 dB during convective rain events. The fourth step determines the RWP calibration constant for one radar beam (called the "reference" beam) by comparing uncalibrated RWP reflectivity factors at 500 m above the ground to 1-min resolution surface disdrometer reflectivity factors. The last step uses the calibrated reference beam reflectivity factor to calibrate the other radar beams during precipitation. There are two key findings. The RWP sensitivity decreased approximately 3-to-4 dB/year as the hardware aged. This drift was slow enough that the reference calibration constant can be estimated over 3-month intervals using episodic rain events. Calibrated moments are available on the DOE ARM data archive and Python processing code is available on a public GitHub repository.

1 Introduction

Ultra High Frequency (UHF) band (900 – 1290 MHz) radar wind profiler (RWP) technology was developed in the 1980s by the U.S. National Oceanic and Atmospheric Administration (NOAA) Aeronomy Laboratory and Wave Propagation Laboratory to study the horizontal wind motions from near the surface to approximately 5 km above ground level (Ecklund et al., 1988; Angevine et al., 1996, 1998; Carter et al., 1995). When raindrops are not in the radar resolution volume, the radar return power during this "clear-air" condition is due to Bragg scattering from changes in refractive index caused by temperature and humidity gradients (Gage and Balsly, 1978). When raindrops are in the radar resolution volume, Rayleigh

https://doi.org/10.5194/egusphere-2022-1405
Preprint. Discussion started: 10 January 2023

scattering dominates the return signal providing vertical structure of precipitation without any signal attenuation (Rogers et al., 1993).

At the radar measurement level, radars measure the return signal power as a function of range. For meteorological applications, the signal power needs to be converted to radar reflectivity factor. In general, there are two methods to convert signal power to radar reflectivity factor. The first method directly converts the measured power and range information into radar reflectivity factor. This method requires rigorous characterisation of every radar subsection using best engineering practices and includes recording the transmitted power in real-time and performing balloon mounted sphere calibrations or pole mounted corner reflector calibrations to characterize the antenna beam pattern and beam pointing hardware (Chandrasekar et al., 2015). For radars that are not end-to-end rigorously characterized (e.g., radar wind profilers), the radar reflectivity factor can be estimated indirectly by using the noise relative signal power (i.e., signal-to-noise ratio SNR) and an external reference to determine the radar calibration constant. For vertically pointing radars, the external reference has come from near-by surface disdrometer observations (Gage et al., 2000; Williams et al., 2005) and from satellite radar statistics (Protat et al., 2011; Kollias et al., 2019; Hartten et al., 2019; Protat et al., 2022).

Since RWPs were originally designed for horizontal wind profile measurements, the NOAA Doppler velocity power spectra processing routines were optimized to estimate mean radial velocity and did not estimate radar reflectivity factor (Merritt, 1995). Even today, real-time processed NOAA RWP datasets do not estimate radar reflectivity factor, but include the spectrum moments of SNR, mean radial velocity, spectrum width, and noise power (NOAA, 2022). The radar reflectivity factor is estimated from SNR as shown in Gage et al. (1994, 2000) and described in more detail in Tridon et al. (2013) and Hartten et al. (2019). One limitation of RWP signal processing routines is that increased noise power occurs at range gates that have large backscattered signal power. This over-estimated noise power leads to under-estimated SNR, which leads to under-estimated radar reflectivity factor. The elevated noise power in RWPs was discussed in Tridon et al. (2013) and mitigated by using the measured noise power at far range gates as a new noise power at all range gates. The adjusted SNR is then used to estimate the radar reflectivity factor. The work presented herein builds on the concepts discussed in Tridon et al. (2013), but includes additional SNR biases not discussed in that work. Specifically, this study includes signal power biases due to Nyquist velocity aliasing and coherent integration filtering. Also, this study uses a daily median noise power in the adjusted SNR estimate to account for radio frequency interference (RFI) that sporadically increases noise power estimates and to account for RWP operating modes that do not have range gates sampling above intense precipitation such that the noise power is still biased high at the "far" range gates.

As discussed above, an external reference is needed to determine a radar calibration constant and this study uses surface disdrometer reflectivity factors to calibrate RWP radar reflectivity factors obtained at 500 m. The calibration procedure includes shifting the time-series data to account for vertical and spatial separation between the measurement locations. An overarching aim of this study is to standardize the RWP signal processing steps to remove known biases in radar reflectivity factor estimates and provide those codes to the radar community on a public repository.

https://doi.org/10.5194/egusphere-2022-1405
Preprint. Discussion started: 10 January 2023

The radar and disdrometer datasets used in this study are described in Section 2 (Data Sets). Spectrum adjustment methods are discussed in Section 3 (Methods) and include adjustments due to Nyquist velocity aliasing, coherent integration filtering, and increased noise power. Section 3 also includes calibration methods derived from surface disdrometer observations. In Section 4 (Results), the radar calibration constant is shown to vary over an 8-year dataset with decreased sensitivity caused by degrading hardware and sudden increases in sensitivity due to installing new hardware. Conclusions are presented in Section 5.

2 Data Sets

This study uses radar observations from a UHF-band radar wind profiler (RWP) operating at 915 MHz and a surface disdrometer located at the US Department of Energy (DOE) Atmospheric Radiation Measurement (ARM) program (Mather and Voyles, 2013) Southern Great Plains (SGP) Central Facility in northern Oklahoma, USA, from 22-March-2011 to 18-August-2019. All datasets used in this study are available online using the ARM Data Discovery Tool (ARM 1998a, 1998b, 1998c, 1998d, 2011).

2.1 Radar Wind Profiler

The ARM SGP Central Facility RWP was a Vaisala Meteorological Systems Inc. wind profiler (Muradyan and Coulter, 2020) and is a commercial version of the NOAA UHF wind profiler developed under an industry-government 1991 Cooperative Research and Development Agreement (CRADA) (Vaisala News, 2002). From 22-March-2011 to 31-March-2014, the RWP operated in a *precipitation mode* observing only in the vertical direction. The precipitation mode sampled the atmosphere with a short- and long-pulse yielding low-sensitivity short-range measurements and high-sensitivity long-range measurements, respectively. On 1-April-2014, a *wind mode* was added to the RWP and consisted of transmitting pulses in three different directions in order to estimate the horizontal wind as a function of height. The RWP collected data in both precipitation and wind modes for 5 years. On 11-March-2019, the wind mode operating parameters changed and on 19-August-2019, the RWP hardware failed and was eventually replaced with a wind profiler produced by a different radar manufacturer. The LAP-3000 RWP can only collect data in one beam direction with one pulse configuration at a time. Thus, during the 2011-to-2014 period, the radar alternated between two vertically pointing precipitation mode radar beams, requiring approximately 5 seconds to collect both beams of data. During the 2014-to-2019 period, the radar sequentially collected data in five unique radar beams (i.e., two precipitation mode beams and three wind mode beams), requiring approximately 25 seconds to complete one observation cycle. Table 1 lists pertinent RWP operating parameters for both modes.

Between 2011 and 2019, the RWP had two hardware failures, which implies that three different hardware configurations were deployed during this 8-year period. Since calibration constants change with ageing and changing hardware, the RWP dataset is divided into five calibration periods as listed in Table 2.

https://doi.org/10.5194/egusphere-2022-1405
Preprint. Discussion started: 10 January 2023

Table 1. Pertinent RWP operating parameters (SGP, Central Facility, 22-March-2011 through 18-August-2019).

Operating Frequency [MHz]	915				
Operating Wavelength [m]	0.328				
	Precip. Short-Pulse	Precip. Long-Pulse	Wind Mode		
Observation Start Date	22-March-2011	22-March-2011	1-April-2014		
Observation End Date	18-August-2019	18-August-2019	10-March-2019		
			BeamV	BeamA	BeamB
Pulse duration () [ns]	417	2833	708	708	708
Range Resolution [m]	62.5	425	106	106	106
Distance between Range Gates [m]	125 then 62.5*	212.5	62.5	62.5	62.5
Number of Range Gates	75 then 150*	75	60	60	60
Range to First Gate [m]	327	327	373	373	373
Range to Last Gate [km]	9.6	16.0	4.0	4.0	4.0
Elevation Angle [degree]	90	90	90	77	77
Azimuth Angle [degree]	22	22	22	22	292
Inter-pulse Period (Tipp) [µs]	100	120	41	41	41
Number of Coherent Integrations (N_{coh})	56	34	200	200	200
Number of points in spectrum (N_{pts})	128	128	64	64	64
Number of Averaged spectra (N_{spc})	3	4	12	12	12
Nyquist Velocity ($V_{Nyquist}$) [m s^{-1}]	14.6	19.6	9.99	9.99	9.99
Velocity resolution (v) [m s^{-1}]	0.228	0.306	0.312	0.312	0.312
Dwell^{+} [s]	2.2	2.1	6.3	6.3	6.3

* Distance between range gates and the number of range gates changed on 4-April-2014

$^{+}$ Dwell is the time needed to transmit all pulses: Dwell = $\left(T_{ipp} N_{coh} N_{pts} N_{spc}\right)$ [s]

https://doi.org/10.5194/egusphere-2022-1405
Preprint. Discussion started: 10 January 2023

Table 2. RWP operating periods with consistent hardware

Period	Start	End	Hardware Version	Operating Modes
A	22-March-2011	31-March-2014	Radar hardware #1	Precipitation
B	1-April-2014	14-July-2015	Radar hardware #1	Precipitation and Wind
-	15-July-2015	24-Sept-2015	Hardware failure	No data collected
C	25-Sept-2015	10-April-2017	Radar hardware #2	Precipitation and Wind
-	11-April-2017	5-June-2017	Hardware failure	No data collected
D	6-June-2017	10-March-2019	Radar hardware #3	Precipitation and Wind
E	11-March-2019	18-August-2019	Radar hardware #3	Precipitation

2.2 Surface Disdrometer

A 2-dimensional video disdrometer (VDIS) manufactured by Joanneum Research, in Graz, Austria (Schönhuber et al., 2008), was deployed about 100 m from the RWP at the SGP Central Facility (Wang et al., 2021; ARM, 2011). The 2DVD uses two orthogonal pointing cameras in the horizontal plane to detect raindrops falling through a 10 cm square opening and then estimates the raindrop number concentration with a 1-minute temporal resolution (Tokay et al., 2001, 2013). Radar reflectivity factors assuming Rayleigh scattering were calculated using PyDisdrometer routines (Hardin and Guy, 2014) as used in previous studies using 2DVD observations (Giangrande et al., 2019).

3 Methods

The ARM RWP records the raw Doppler velocity power spectra and real-time spectrum moments are calculated on the RWP host computer using the RWP manufacturer processing routines. These raw spectrum moments are labelled "a0" using ARM's file naming protocols (ARM, 2022) and saved on the ARM archive in netCDF format (ARM 1998a, 1998b, 1998c, 1998d). The recorded spectrum moments are not calibrated and do not include a radar reflectivity factor estimate. To illustrate the motivation for reprocessing the recorded spectra, Fig. 1 shows time-height cross-sections of recorded moments of signal-to-noise ratio (SNR^{a0}) [dB] (Fig. 1a), mean radial velocity (V_{mean}^{a0}) [m s^{-1}] (Fig. 1b), and spectrum noise power (P_{noise}^{a0}) [dB] (Fig. 1c) for a rain event on 7-June-2018 using the precipitation short-pulse mode. Examination of the SNR^{a0} time-height structure in Fig. 1a suggests convective rain near 11:45 to 12:00 UTC followed by stratiform rain after about 12:15 UTC. There are a couple questionable features in this figure between 11:35 and 12:10 UTC that raise concern about the quality of the recorded spectrum moments. First, the SNR^{a0} contains speckles of low magnitude SNR above the height of about 3 km. Second, the V_{mean}^{a0} has large, unphysical jumps in velocity over several range gates and several profiles due to Nyquist velocity aliasing. Third, the spectrum noise power P_{noise}^{a0}, which is the denominator in estimating SNR, has large and

https://doi.org/10.5194/egusphere-2022-1405
Preprint. Discussion started: 10 January 2023

variable magnitudes at nearly all range gates. The first two features are due to the on-line processing codes incorrectly estimating the spectrum moments, while the third feature is due to signal power leaking during the Fast Fourier Transform (FFT) operation with the leaked power being deposited as noise power across the whole Doppler velocity power spectrum.

This section describes the five step RWP calibration procedure. First, the raw Doppler velocity power spectra are adjusted to account for both Nyquist velocity aliasing (see Section 3.1.1) and coherent integration filtering (see Section 3.1.2). Second, the spectrum moments are recalculated (see Section 3.1.3). Third, the recalculated SNR is increased to account for leaking signal power into the noise power to yield an adjusted signal-to-noise ratio (see Section 3.2). Fourth, a calibration constant is determined for the precipitation short-pulse radar beam (defined as the "reference" beam) by comparing radar reflectivity factors with surface disdrometer observations (see Section 3.3). The last step determines relative calibration offsets between the reference beam and the other four radar beams. The calibration constant for each beam is the combination of the reference beam calibration constant and that beam's relative calibration offset (see Section 3.4). To differentiate between the real-time processed moments and the reprocessed moments, the former estimates are labelled "a0" and the latter are labelled "revised".

https://doi.org/10.5194/egusphere-2022-1405
Preprint. Discussion started: 10 January 2023

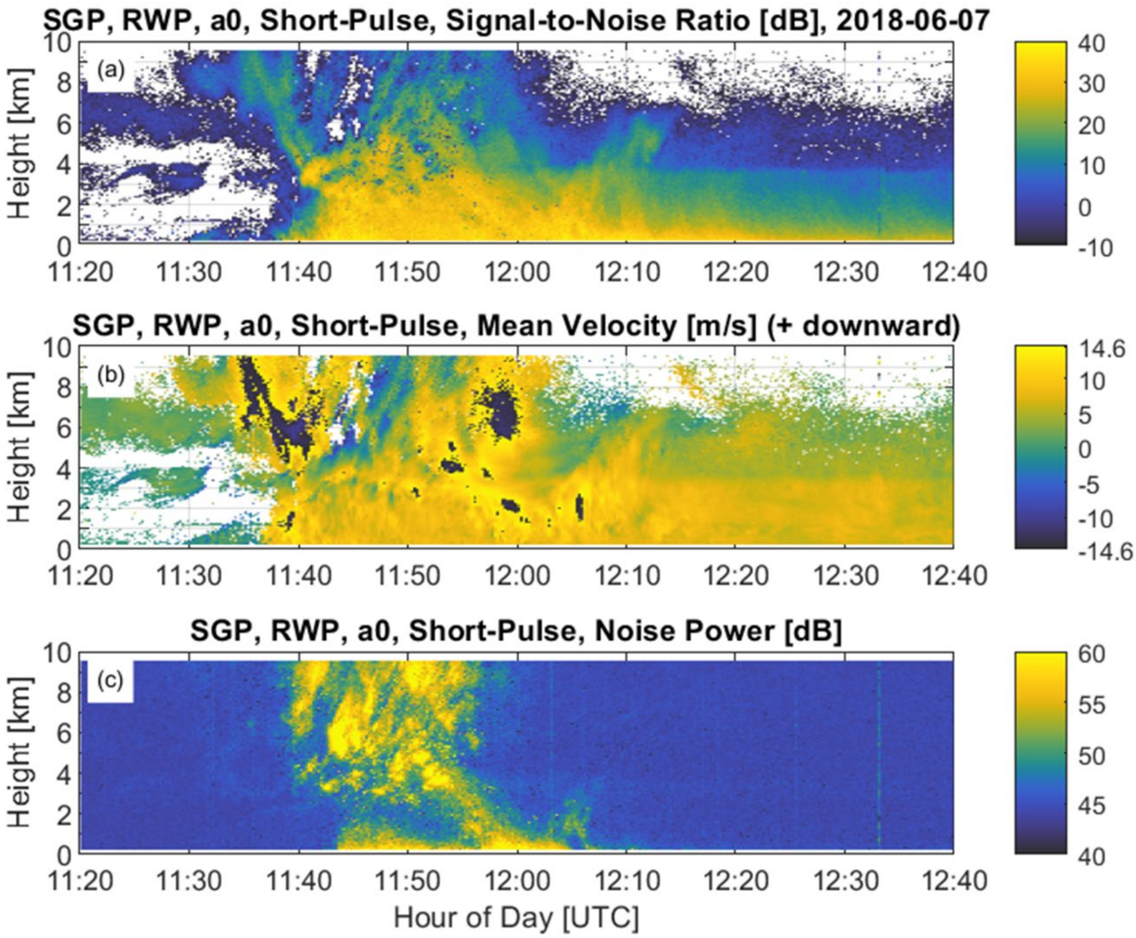

Figure 1. Radar wind profiler (RWP) spectrum moments calculated with the real-time processing algorithms and downloaded from the DOE ARM archive. RWP is located at the SGP Central Facility. Observations are from the vertically pointing beam using the precipitation short-pulse mode on 07-June-2018 between 11:20 to 12:40 UTC. (a) Signal-to-Noise Ratio (SNR) [dB], (b) mean radial velocity with positive values moving downward toward the radar [m s^{-1}], and (c) spectrum noise power [dB].

3.1 Doppler Velocity Power Spectrum Adjustments and Calculating Spectrum Moments

This subsection describes three processing steps: 1) spectrum adjustments due to Nyquist velocity aliasing, 2) spectrum adjustments due to coherent integration, and 3) recalculating the spectrum moments.

3.1.1 Eliminating Nyquist Velocity Aliasing

Nyquist velocity aliasing is when the target radial velocity exceeds the Nyquist velocity and the target appears to be moving in the opposite direction. One velocity aliasing mitigation technique is to concatenate two Doppler velocity spectra to remove the artificial boundary at the Nyquist velocity (Williams et al., 2018). Figure 2 shows an example of velocity aliasing between 5 and 8 km using precipitation short-pulse mode Doppler velocity power spectra for a single profile collected on 7-

https://doi.org/10.5194/egusphere-2022-1405
Preprint. Discussion started: 10 January 2023

June-2018 at 11:58:20 UTC. The original power spectra are plotted within the Nyquist velocity ($V_{Nyquist}$) range of $\pm$14.6 m s^{-1}, with downward motions having positive values consistent with raindrop gravitational fall speeds. The original spectra are copied in Fig. 2 to visualize and to mitigate Nyquist velocity aliasing. Specifically, the downward (upward) motions between 0 and 14.6 m s^{-1} are copied to upward (downward) motions between 29.2 to 14.6 m s^{-1}. The red circles in Fig. 2 designate real-line mean radial velocity moments V_{mean}^{a0}. Note the jump in V_{mean}^{a0} near 5.5 km from downward to upward motion, which is due to the assumption in the real-line signal processing routines that all signal power is within the Nyquist interval of $\pm V_{Nyquist}$.

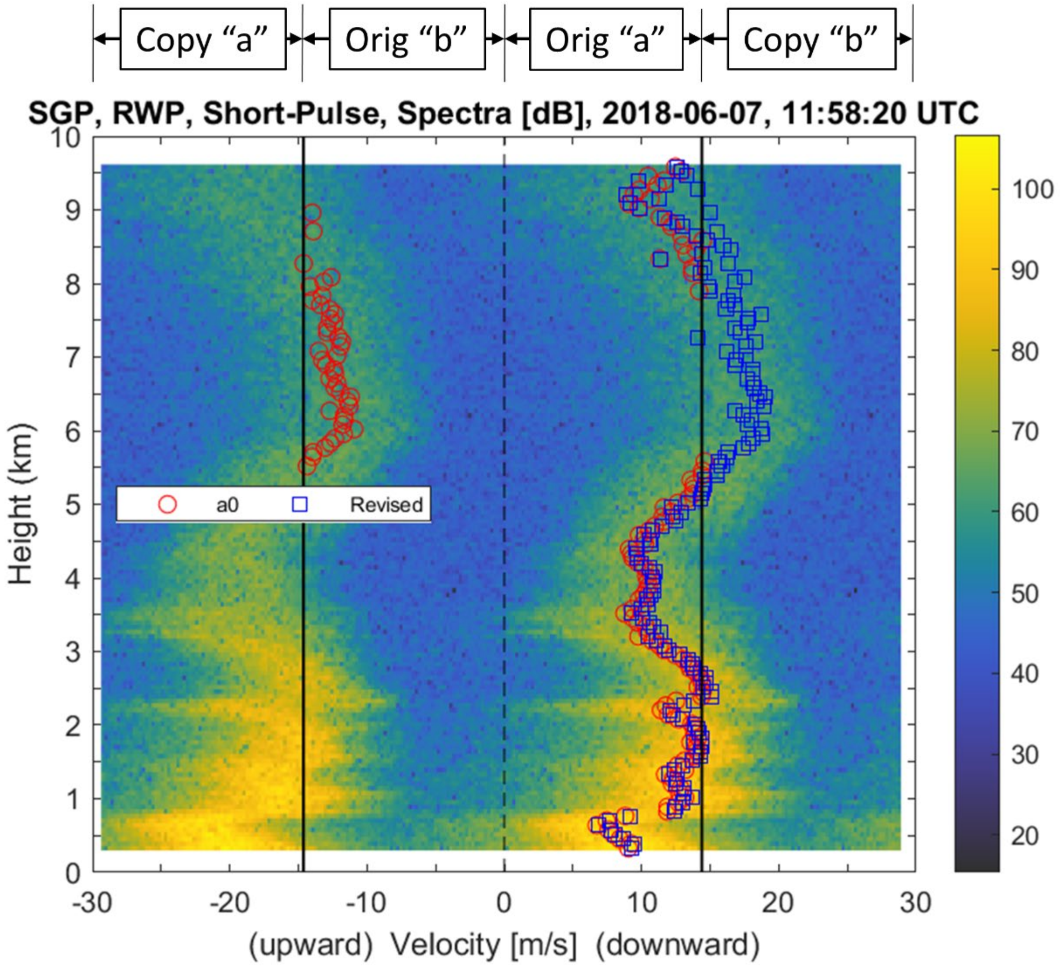

Figure 2. Spectra profile at time 11:58:20 [UTC] on 7-June-2018. Downward velocities have positive values and are approaching the ground-based radar. Original spectra are plotted between Nyquist velocities -14.6 and 14.6 m s^{-1} and are indicated with solid lines. The portion of original spectra with downward motion is copied to be more upward than the Nyquist velocity (i.e., portion labelled “a”) and the portion of original spectra with upward motion is copied to be more downward than the Nyquist velocity (i.e., portion labelled “b”). Red circles designate real-time estimated mean radial velocities and blue squares denote revised mean radial velocities. Dashed line indicates 0 m s^{-1} velocities. Spectra magnitudes are uncalibrated spectral power density units expressed in decibels (i.e., $10log[S(v)]$ with units dB).

https://doi.org/10.5194/egusphere-2022-1405
Preprint. Discussion started: 10 January 2023

For spectra that have velocity aliasing, the SNR is biased low when using the assumption that all of the signal power is within $\pm V_{Nyquist}$. This issue can be visualized in Fig. 3 and shows individual spectra at 6 km (Fig. 3a) and 3 km (Fig. 3b). The signal-to-noise ratio can be estimated using (Riddle et al., 2012):

$$SNR = 10log\left[\frac{\sum_{v_{start}}^{v_{end}}[S(v_i)-\bar{n}]\Delta v}{\bar{n}N_{pts}\Delta v}\right] \quad \text{[dB]} \quad (1)$$

where v_{start} and v_{end} [m s^{-1}] are the integration limits indicating the start and end velocities of the power spectrum $S(v_i)$ containing signal power [uncalibrated power per (m s^{-1})], v_i is the velocity bin, Δv [m s^{-1}] is the velocity bin resolution, $\bar{n}$ is the spectrum mean noise level [uncalibrated power per (m s^{-1})] (Hildebrand and Sekhon, 1974), and N_{pts} is the number of points in the spectrum. The integration limits in (1) are estimated by finding the maximum value in the spectrum and moving to the left and right until the spectrum magnitude drops below the mean noise level $\bar{n}$ (Carter et al., 1995). In Fig. 3b, the maximum spectrum value occurs within the Nyquist interval and is near 10 m s^{-1} downward. For the real-time processing routine, the v_{start} integration limit is near 0 m s^{-1} and the v_{end} limit stops at the Nyquist velocity of 14.6 m s^{-1} because of the assumption that all power occurs within the Nyquist velocity interval. The spectrum between these integration limits is shaded red and labelled *a0 spectrum* in Fig. 3. The revised processing estimates the integration limits using the same search technique, except it uses the extended spectrum illustrated in Fig. 2. For the revised processing, the v_{start} integration limit is the same as the real-time processing routine, but the v_{end} limit extends past the Nyquist velocity and ends where the spectrum crosses the mean noise level near 20 m s^{-1} downward. The different integration limits cause the real-time processing method to underestimate both the SNR and mean radial velocity relative to the dealiased method by 0.2 dB and 0.2 m s^{-1}, respectively. As will be seen in the next section, including the incoherent averaging filtering effects will increase these differences.

In Fig. 2, between 5.5 and 9 km, V_{mean}^{a0} appears to have upward motion. This is because the maximum spectrum magnitude is occurring outside the $\pm V_{Nyquist}$ boundaries and the peak velocity is aliased. In Fig. 3a, the real-time processing routine has found the integration limits of -14.6 (at the Nyquist boundary) and approximately -5 m s^{-1}. This *a0 spectrum* region is shaded red in Fig. 3a. In contrast, the revised processing uses the dealiased spectrum and finds integration limits of approximately 11 and 24 m s^{-1} downward (spectrum region with blue strips). The different integration limits produce significantly different mean radial velocities of $V_{mean}^{a0} = -10.5$ m s^{-1} and $V_{mean}^{revised} = 17.9$ m s^{-1}.

https://doi.org/10.5194/egusphere-2022-1405
Preprint. Discussion started: 10 January 2023

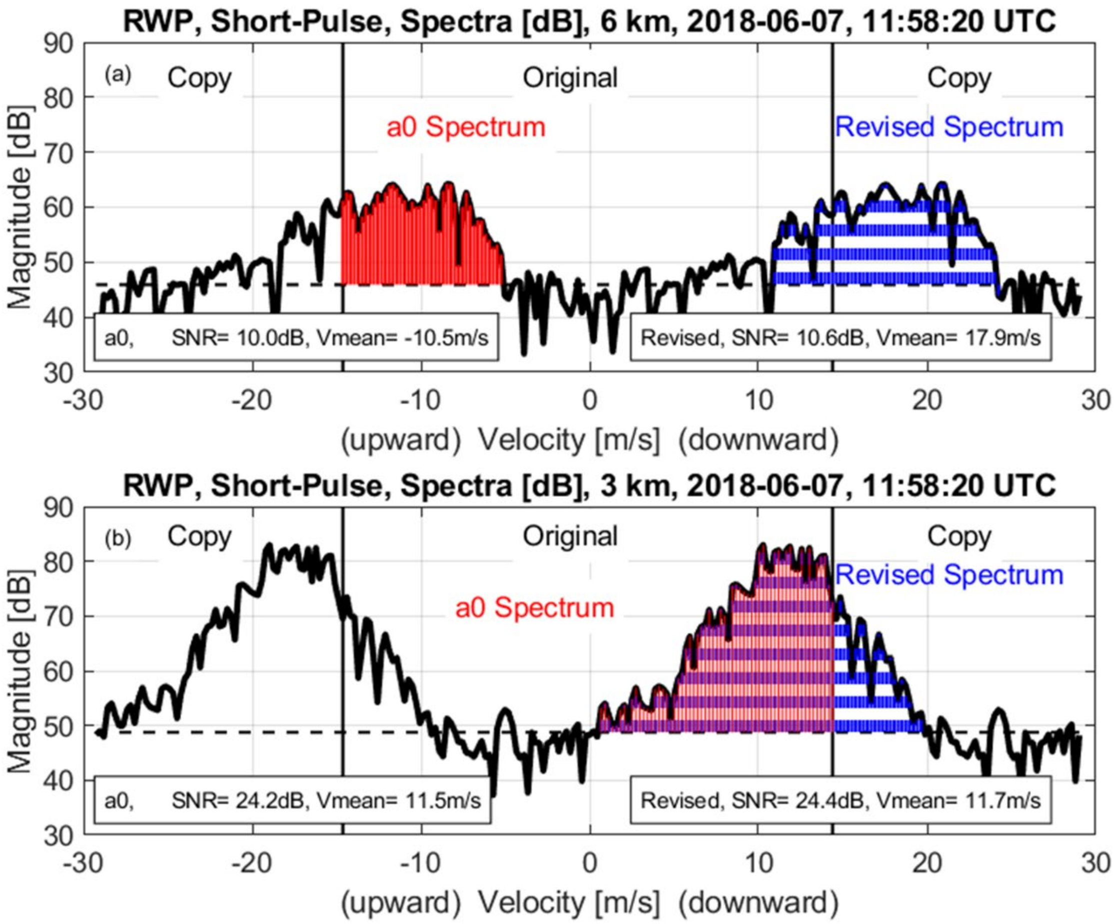

Figure 3. Example of integration limits used in the real-time and revised spectrum moment estimation algorithms. Uncalibrated spectral power density expressed in decibels [dB] for profile at 11:58:20 [UTC] on 7-June-2018 at (a) 6 km and (b) 3 km. Red shading and blue horizontal bars indicate spectral power density used to estimate *a0* and revised moments, respectively.

3.1.2 Coherent Integration Adjustment

Coherent integration is a signal processing technique that accumulates the radar measured in-phase and quadrature voltages (aka, I and Q voltages) over consecutive transmitted pulses. Signals that are slowly varying over the accumulation interval are said to be coherent and their accumulation causes an increase in signal power. Conversely, accumulating high frequency oscillations, including noise fluctuations, produce smaller magnitude accumulated powers. Thus, coherent integration increases radar detection by acting as a low-pass filter that increases low-frequency signal powers and decreases high-frequency noise power (Farley, 1985).

Coherent integration is also known as time-domain averaging (TDA) and is implemented by changing the number of coherent integration samples N_{coh}, which changes the effective time between transmitted samples and decreases the Nyquist velocity using:

https://doi.org/10.5194/egusphere-2022-1405
Preprint. Discussion started: 10 January 2023

$$V_{Nyquist} = \left(\frac{\lambda}{4}\right)\left(\frac{1}{N_{coh}T_{IPP}}\right) \tag{2}$$

where λ is the radar operating wavelength and T_{IPP} is the inter-pulse period (aka, time between transmitted pulses). Coherent integration also applies a boxcar filter to the I and Q voltage time-series samples before integrating, which is equivalent to applying a low-pass filter to the integrated time-series. Since coherent integration is performed before computing the FFT on the complex I and Q voltage samples, the low-pass filter manifests as a reduction in FFT signal power magnitude as a function of velocity v_i and has the form (Schmidt et al., 1979):

$$S_{recorded}^{signal}(v_i) = S_{expected}^{signal}(v_i)\left[\frac{sin^2\left[\frac{\pi\left(\frac{v_i}{\Delta v}\right)}{N_{pts}}\right]}{\left(N_{coh}^2\right)\left(sin^2\left[\frac{\pi\left(\frac{v_i}{\Delta v}\right)}{N_{coh}N_{pts}}\right]\right)}\right] \tag{3}$$

where $S_{recorded}^{signal}(v_i)$ is the recorded signal power spectrum at velocity bin v_i, $S_{expected}^{signal}(v_i)$ is the expected signal power spectrum without any time-domain low-pass filtering effects, and N_{pts} is the number of complex I and Q samples after coherent integration, which is also the number of velocity bins in the power spectrum after performing the FFT calculation. The ratio $\left(\frac{v_i}{\Delta v}\right)$ yields integers from $\frac{-N_{pts}}{2}$ to $\frac{N_{pts}}{2}$. Note that the low-pass filter response function (the expression within the square brackets in (3)) has a magnitude of one when $v_i = 0$ and decreases with increasing v_i.

The impact of the TDA low-pass filter can be mitigated by applying a correction factor to the recorded Doppler velocity power spectra. Since the low-pass filter only affects coherent signals, the correction factor should only be applied to the signal portion of the power spectrum and not to the random noise power. Thus, the TDA corrected power spectrum $S_{TDA}(v_i)$ is estimated using:

$$S_{TDA}(v_i) = \left[S(v_i) - \bar{n}\right]\left[\frac{\left(N_{coh}^2\right)\left(sin^2\left[\frac{\pi\left(\frac{v_i}{\Delta v}\right)}{N_{coh}N_{pts}}\right]\right)}{sin^2\left[\frac{\pi\left(\frac{v_i}{\Delta v}\right)}{N_{pts}}\right]}\right] + \bar{n} \tag{4}$$

where $S(v_i)$ is the recorded Doppler velocity power spectrum. For the precipitation short-pulse mode, the correction factor magnitude (the expression in the square brackets in (4)) at $\pm V_{Nyquist}$ is 2.47 in natural units as in equation (4) or 3.9 dB in decibels. Figure 4 shows the recorded power spectra shown in Fig. 3 with the revised spectrum corrected for the TDA filtering expressed in (4). The SNR and mean radial velocity moments for real-time moments and the revised spectrum are listed in Fig. 4. Comparing the non-TDA and TDA corrected moments for the dealiased spectra at 6 km (see Figs. 3a and 4a, respectively), indicates the SNR increased 7.4 dB and the mean radial velocity became more downward by 1.6 m s^{-1} when including the TDA filter correction. Note that the difference in *a0* and TDA corrected mean radial velocities at 6 km is 30 m s^{-1} (see Fig. 4a) and is not a multiple of $\pm 2V_{Nyquist}$ ($\pm$29.2 m s-1). This indicates that simple integer $\pm 2V_{Nyquist}$ adjustments, as proposed by Tridon et al. (2013), will not account for improper integration limits used in the real-time processing routines.

https://doi.org/10.5194/egusphere-2022-1405
Preprint. Discussion started: 10 January 2023

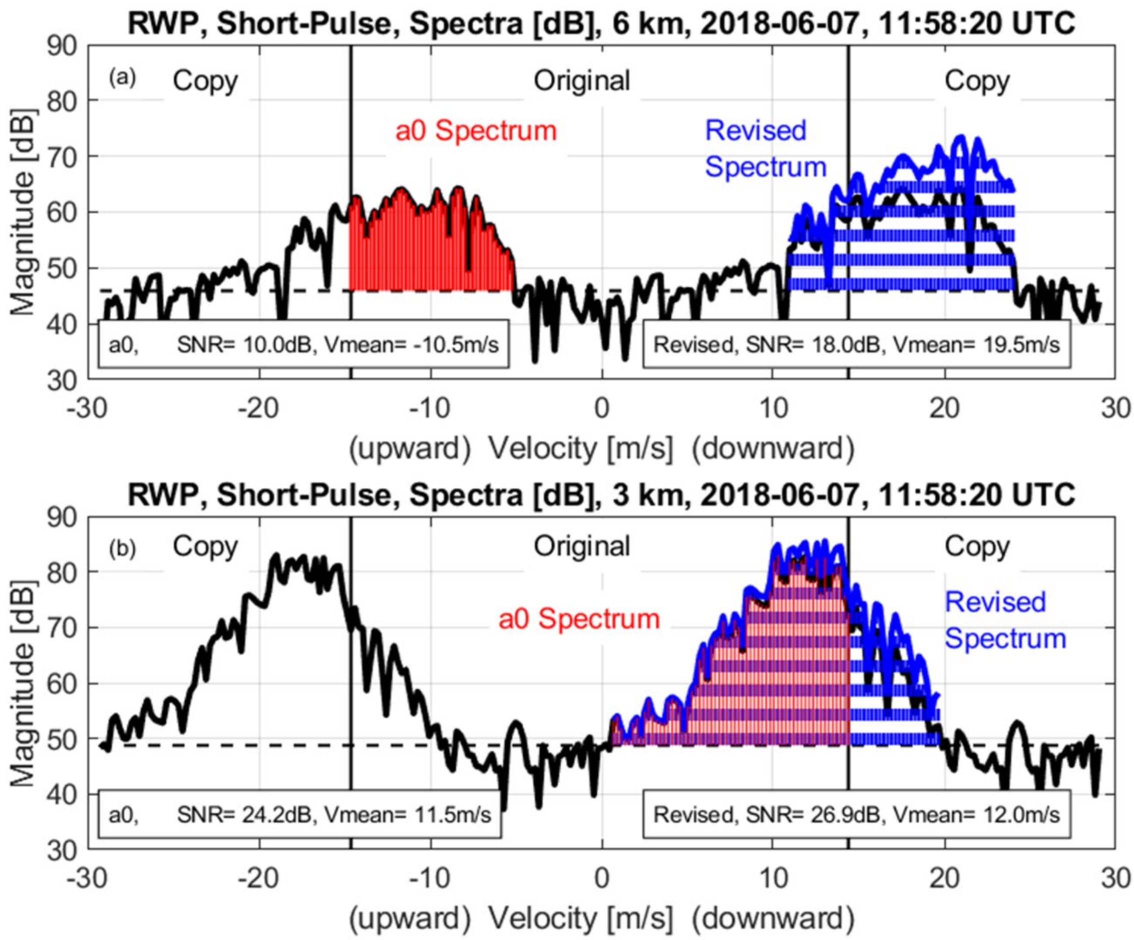

Figure 4. Similar to Fig. 3, except the revised spectrum (blue line and blue horizontal bars) have been TDA corrected using (4).

3.1.3 Calculating Spectrum Moments

After adjusting the recorded spectrum due to Nyquist velocity aliasing and coherent integration effects, the spectrum moments are calculated following the method and equations presented in Williams et al. (2018) Appendix A and include revised estimates of spectrum signal power ($P_{signal}^{revisded}$) [dB], spectrum noise power ($P_{noise}^{revised}$) [dB], signal-to-noise ratio ($SNR^{revised}$) [dB], spectrum mean radial velocity ($V_{mean}^{revised}$) [m s^{-1}], spectrum standard deviation ($\sigma^{revised}$) [m s^{-1}], spectrum width ($W^{revised} = 2\sigma^{revised}$) [m s^{-1}], spectrum skewness, and spectrum kurtosis. The dealiasing procedure described in Section 3.1.1 produces a spectrum with two peaks. To determine the correct peak, the processing starts at the lowest range gate for each profile and progresses upward. Assuming that the correct peak is determined at the lowest valid range gate, the mean radial velocity from the previous range gate is used to identify the correct peak in the next range gate.

https://doi.org/10.5194/egusphere-2022-1405
Preprint. Discussion started: 10 January 2023

3.2 Signal-to-Noise Ratio (SNR) Adjustment

Due to increased noise power in the recalculated spectra, the third calibration processing step increases the magnitude of $SNR^{revised}$. The *a0* processed noise power P_{noise}^{a0} shown in Fig. 1c had increased magnitudes at nearly all range gates during the convective rain event between approximately 11:35 and 12:10 UTC. This increased noise power is not expected for a pulse radar because noise power should be independent of range. However, as the return signal power increases, an increase in noise power is a common feature in RWP spectra because the FFT calculation leaks signal power from a narrow velocity range to the whole velocity range. Though not noticeable in small signal magnitude spectra due to other noise sources, signal power is leaking in every FFT calculation. As the signal power magnitude increases, the FFT leakage causes the spectrum noise power to increase above the noise power produced by other radar noise sources.

The increased noise power causes the measured signal-to-noise ratio to be biased low. To correct for this bias, a reference noise power $P_{noise}^{reference}$ [dB] is determined and an adjusted SNR is estimated using:

$$SNR_{adjusted}^{revised} = SNR^{revised} + P_{noise}^{revised} - P_{noise}^{reference} \quad \text{[dB]} \tag{5}$$

where $SNR^{revised}$ and $P_{noise}^{revised}$ are moments calculated in Section 3.1.3.

The noise power for every spectrum is estimated using the method outlined in Hildebrand and Sekhon (1974). The reference noise power $P_{noise}^{reference}$ is the median noise power derived from all spectra collected on a given day. Figure 5 shows the daily median noise power for the precipitation short-pulse (black plusses) and long-pulse (red crosses) for the 8-year dataset. The jump in daily median noise power in mid-2017 corresponds to the installation of new radar hardware.

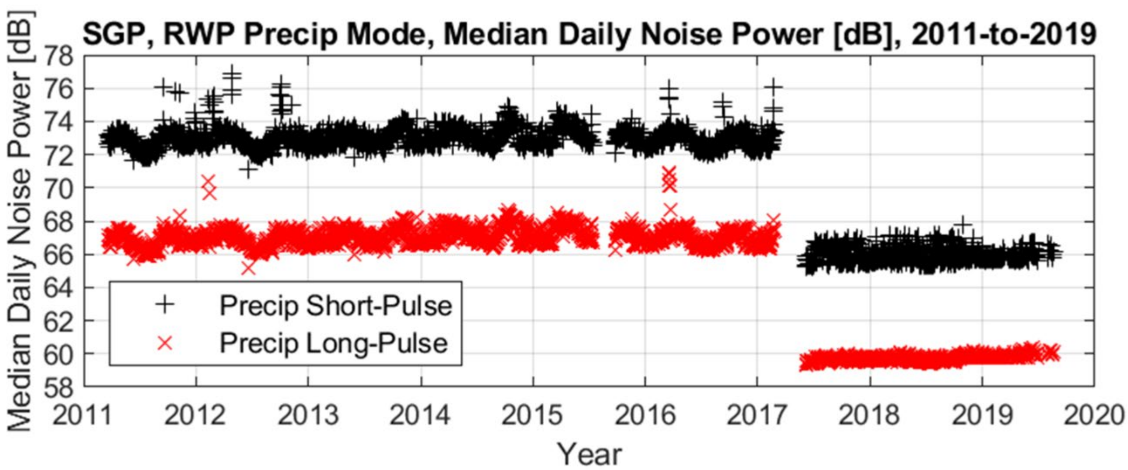

Figure 5. Daily median noise level for the precipitation short-pulse (black plusses) and long-pulse (red crosses) mode for observations between 2011 and 2019.

Figure 6 illustrates the impact of adjusting the signal-to-noise ratio with the reference noise power. Fig. 6a shows the real-time estimated SNR^{a0} (thick line) and P_{noise}^{a0} (thin line) profiles. The large variations in P_{noise}^{a0} between 4 and 5 km appear as large and inverse variations in SNR^{a0}. Figure 6b shows the adjusted signal-to-noise ratio using two methods. The

https://doi.org/10.5194/egusphere-2022-1405
Preprint. Discussion started: 10 January 2023

method described in Tridon et al. (2013) uses the real-time moments (SNR^{a0} and P_{noise}^{a0}) to estimate the adjusted signal-to-noise ratio $SNR_{adjusted}^{a0}$ (thick blue line in Fig. 6b). The method described herein recalculates the moments and then estimates the adjusted signal-to-noise ratio $SNR_{adjusted}^{revised}$ using equation (5) (thin red line). The profile offset in Fig. 6b is due to different reference noise powers used in the two methods. The $SNR_{adjusted}^{a0}$ has more variability than $SNR_{adjusted}^{revised}$, indicating that the revised spectra reprocessing method produces smoother, more vertically consistent, SNR vertical profiles than the Tridon et al. (2013) method.

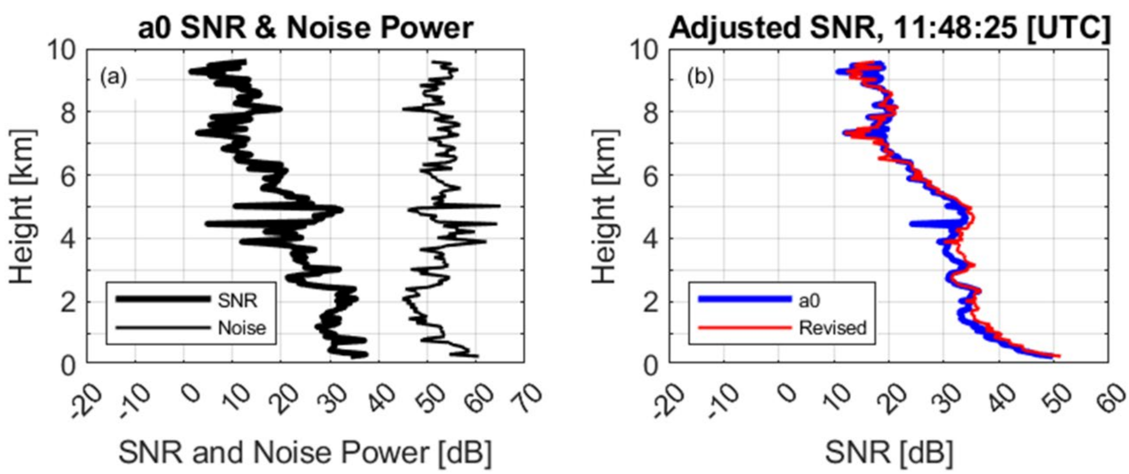

Figure 6. Moment profiles at time 11:48:25 [UTC] on 7-June-2018. (a) SNR and spectrum noise power from real-time spectrum processing routines. (b) Adjusted SNR using the *a0* moments shown in panel (a) (thick blue line) and adjusted SNR using the revised spectral method (thin red line). The adjusted SNR profiles are offset because of different reference noise values.

3.3 Calibrating Reference Beam to Surface Disdrometer

The precipitation short-pulse beam is defined as the RWP reference beam and the radar reflectivity factor $Z^{PrecipShort}$ [dBZ] for this beam is estimated from the adjusted signal-to-noise ratio $SNR_{adjusted}^{PrecipShort}$ using

$$Z^{PrecipShort}(r) = SNR_{adjusted}^{PrecipShort} + 20\log(r) + C^{PrecipShort} \quad \text{[dBZ]} \quad (6)$$

where r [m] is range from the radar and $C^{PrecipShort}$ [dB] is the calibration constant. To estimate the calibration constant $C^{PrecipShort}$, an initial value of $C^{PrecipShort} = 0$ dB is selected and equation (6) is used to estimate the RWP reflectivity factor at all range gates. These initial RWP reflectivity factors at 500 m above ground level are averaged into 1-minute quantities and then compared with the 1-minute surface disdrometer radar reflectivity factors. Using only disdrometer reflectivity factors between 20-to-40 dBZ, the reflectivity factor differences are calculated for RWP lags between ± 4 minutes. Figure 7 shows scatter plots and statistics of mean, standard deviation, and Parson's correlation coefficient for the 7-June-2018 rain event at nine different lags. For this rain event, the distribution in Fig. 7d is selected for calibration because it has the highest Parsons correlation coefficient of 0.95.

https://doi.org/10.5194/egusphere-2022-1405
Preprint. Discussion started: 10 January 2023

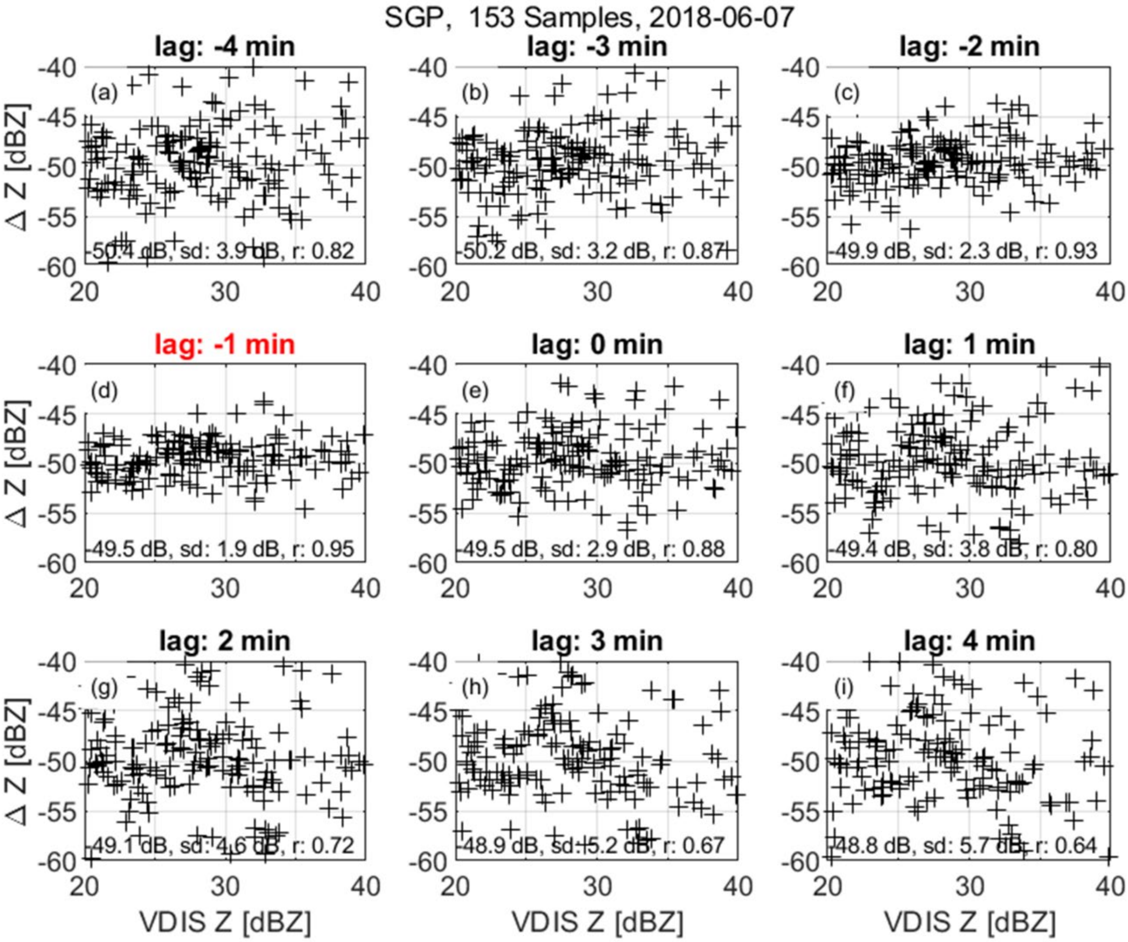

Figure 7. Scatter plots of reflectivity factor differences between RWP precipitation short-pulse mode (with $C^{PrecipShort} = 0$ dB) and surface disdrometer for different minute lags for the rain event on 7-June-2018. Positive lags indicate RWP shifted to later time. Lag times for each panel are (a) -4 min (b) -3 min, (c) -2 min, (d) -1 min (e) 0 min, (f) 1 min, (g) 2 min (h) 3 min, and (i) 4 min. This rain event had 153 minute samples with surface disdrometer reflecticity factor between 20 and 40 dBZ. Each panel indicates rain event mean difference, standard deviation (sd), and Parsons correlation coefficient (r). Panel (d) has the largest Parsons correlation coefficient and is used for calibrating this event. The calibration constant for this event is $C^{PrecipShort} = -49.5$ dB.

Using the calibration constant and lag determined from Fig. 7d (i.e., $C^{PrecipShort}$ =-49.5 dB and -1-minute lag), Fig. 8a shows the time-height cross-section of calibrated RWP precipitation short-pulse mode radar reflectivity factor. Figure 8b shows a time-series of RWP reflectivity factor at 500 m (red crosses) and the surface disdrometer reflectivity factor (black plusses). The blue thin lines in Fig. 8b at 20 and 40 dBZ indicate the reflectivity factor range used for calculating the RWP and disdrometer differences, which are shown in Fig. 8c. Also shown in Fig. 8c are the statistics for this lag, including lag, number of samples, calibration constant, standard deviation, and Parson's correlation coefficient. The standard deviation of 1.9 dB for this event is due to spatiotemporal mismatch between the surface disdrometer and radar sample volume as well as measurement uncertainties of both instruments, and is comparable to 1-to-2 dB measurement uncertainties of side-by-side

https://doi.org/10.5194/egusphere-2022-1405
Preprint. Discussion started: 10 January 2023

surface disdrometers (Tapiador et al., 2017; Wang et al., 2021). Note that the lag is only used in the calibration procedure and not used as a time offset for any other purpose.

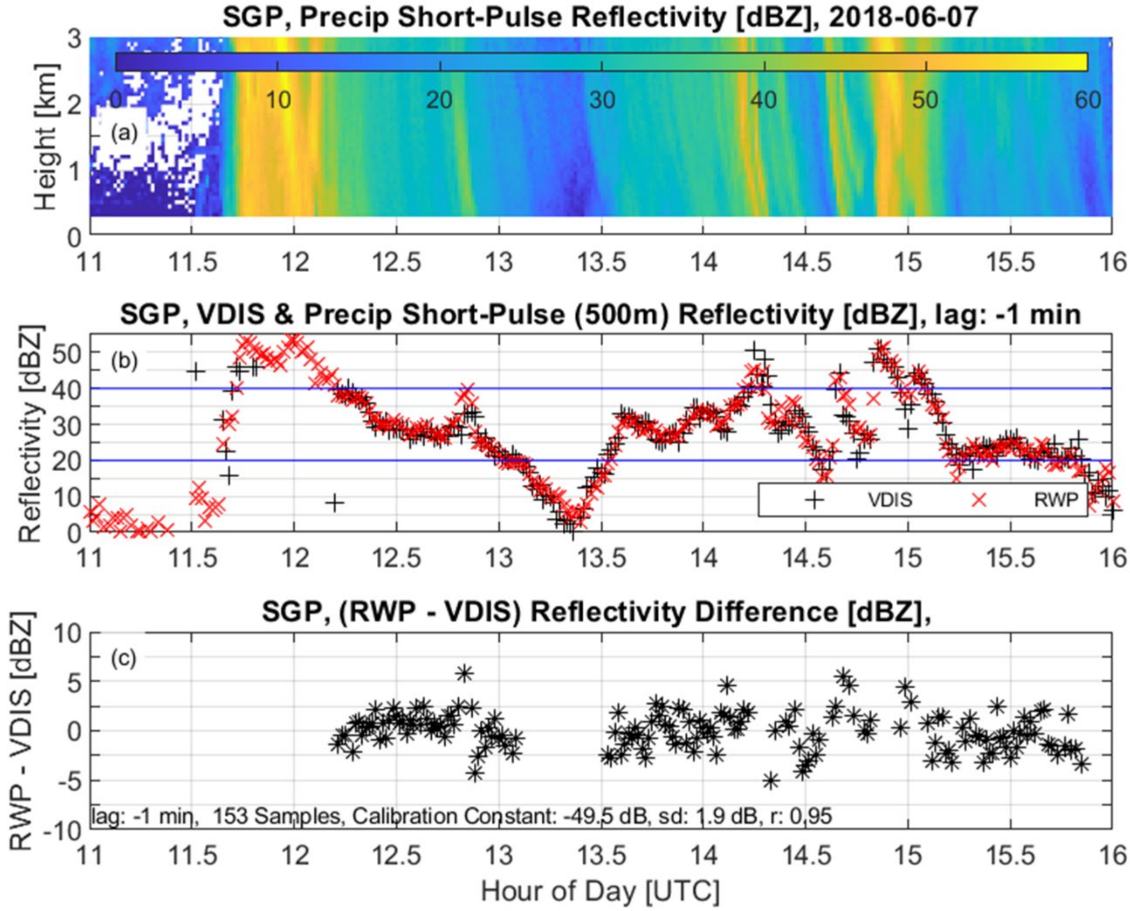

Figure 8. RWP precipitation short-pulse mode and surface disdrometer observations from 7-June-2018 between 11 and 16 UTC. (a) RWP radar reflectivity factor with calibration constant of -49.5 dB, (b) RWP radar reflectivity factor (red crosses) at 500 m range with -1-minute lag and surface 2DVD radar reflectivity factor (black plusses), and (c) reflectivity factor difference (RWP – VDIS) for samples with VDIS reflectivity factor within 20 to 40 dBZ as indicated with blue thin lines in panel (b). Statistics are shown in the bottom panel.

Figure 9 shows improved moments and calibrated reflectivity factors for the same rain event shown in Fig. 1. The top panel (Fig. 9a) shows the revised adjusted signal-to-noise ratio ($SNR_{adjusted}^{PrecipShort}$) and the middle panel (Fig. 9b) shows the revised mean radial velocity ($V_{mean}^{PrecipShort}$). Compared to the *a0* real-time processed moments, the reprocessed moments shown in Figs. 9a and 9b show improved data quality and uniformity. The calibrated radar reflectivity is shown in Fig. 9c.

https://doi.org/10.5194/egusphere-2022-1405
Preprint. Discussion started: 10 January 2023

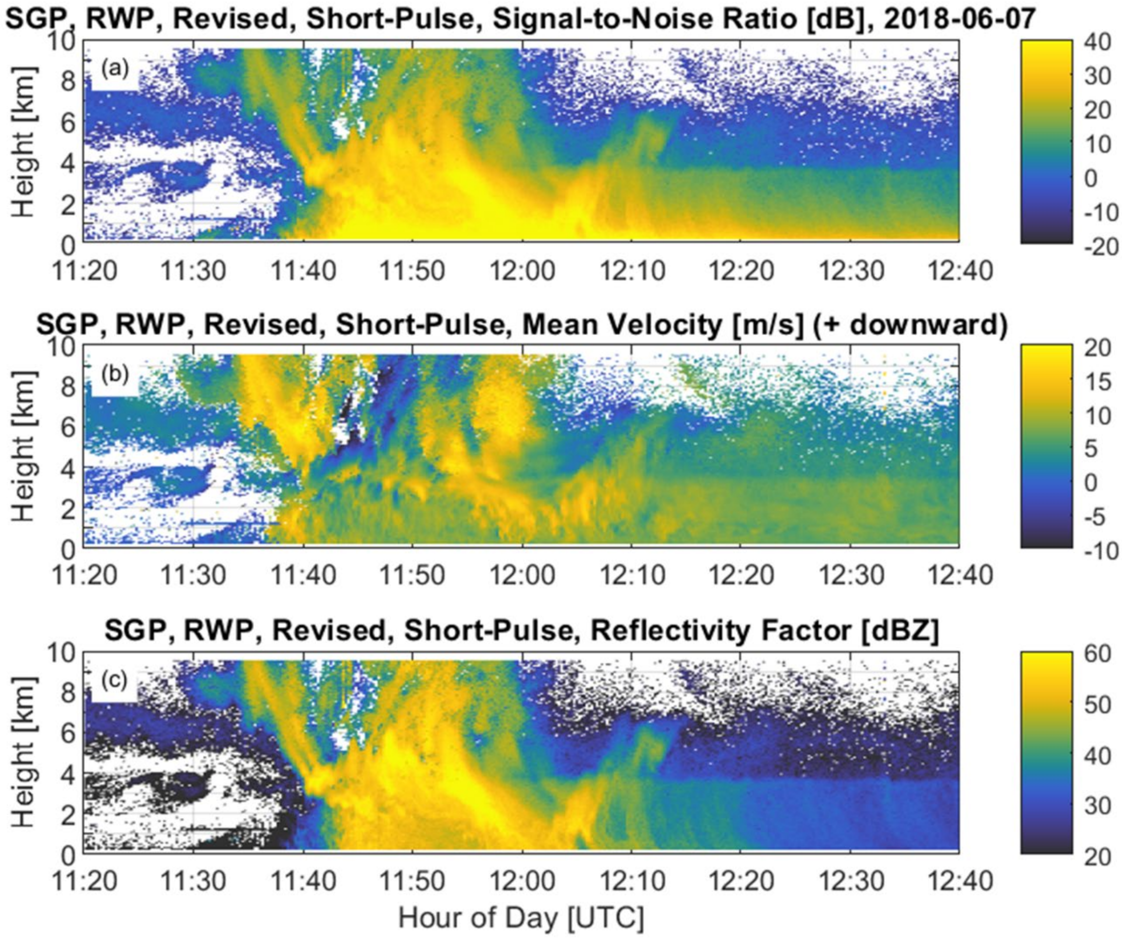

Figure 9. Similar to Fig. 1 except RWP spectrum moments for the precipitation short-pulse mode calculated with the revised processing algorithms. (a) Signal-to-noise ratio $SNR_{adjusted}^{PrecipShort}$ [dB], (b) mean radial velocity $V_{mean}^{PrecipShort}$ [m s^{-1}] with positive values moving downward consistent with raindrop gravitation fall speeds, and (c) surface disdrometer calibrated radar reflectivity factor $Z^{PrecipShort}$ [dBZ].

3.4 Relative Calibration Constants for Other Radar Beams

The radar sensitivity can be adjusted by changing the transmitted pulse length, the number of coherent integrations, and the number of averaged Doppler velocity spectra. Using the precipitation short-pulse mode as the reference beam, the expected relative change in sensitivity for the other four radar beams can be estimated using:

$$C_{relative}^{OtherMode} = 20log\left[\frac{\Delta R^{MUT}}{\Delta R^{PrecipShort}}\right] + 10log\left[\frac{N_{coh}^{MUT}}{N_{coh}^{PrecipShort}}\right] + 5log\left[\frac{N_{spc}^{MUT}}{N_{spc}^{PrecipShort}}\right] \quad (7)$$

where ΔR is the range resolution, N_{coh} is the number of coherent samples, N_{spc} is the number of averaged power spectra, and the superscripts *PrecipShort* and *MUT* represent the precipitation short-pulse mode and the mode under test (MUT), respectively. Using the values from Table 1 and equation (7), Table 3 lists the expected relative sensitivities for the

https://doi.org/10.5194/egusphere-2022-1405
Preprint. Discussion started: 10 January 2023

precipitation long-pulse mode and the wind mode. Note that because all three wind beams use the same operating parameters, they have the same expected relative sensitivity. System losses and variations in antenna gain cause the measured relative sensitivities to deviate from the expected values listed in Table 3.

The reflectivity factor for the other four radar beams follows equation (6) with the addition of the relative calibration constant $C_{relative}^{OtherMode}$ [dB] and is estimated using:

$$Z^{OtherMode}(r) = SNR_{adjusted}^{OtherMode} + 20\log(r) + \left(C^{PrecipShort} - C_{relative}^{OtherMode}\right) \quad \text{[dBZ]}. \qquad (8)$$

The negative sign in the bracketed term is because a positive $C_{relative}^{OtherMode}$ indicates this mode is more sensitive than the precipitation short-pulse mode and will produce a larger $SNR_{adjusted}^{OtherMode}$ for the same radar reflectivity factor. Note that weaker radar reflectivity factors will be detected at further ranges at the expense of possible receiver saturation from large reflectivity factor targets at close range.

Table 3. Expected relative sensitivity of other radar beams compared with the reference precipitation short-pulse beam. Relative sensitivity has three terms in equation (7) and is dependent on range resolution ΔR, coherent integration N_{coh}, and number of averaged Doppler velocity power spectra N_{spc}.

Relative Sensitivity		Precipitation Mode	Wind Mode		
		Long-Pulse	BeamV	BeamA	BeamB
Elevation angle [degree]		90°	90°	77°	77°
Azimuth angle [degree]		22°	22°	22°	292°
$20log\left[\frac{\Delta R^{MUT}}{\Delta R^{precipShort}}\right]$	[dB]	16.5	4.6		
$10log\left[\frac{N_{coh}^{MUT}}{N_{coh}^{PrecipShort}}\right]$	[dB]	-2.2	5.5		
$5log\left[\frac{N_{spc}^{MUT}}{N_{spc}^{PrecipShort}}\right]$	[dB]	0.6	3.0		
$C_{relative}^{OtherMode}$	[dB]	14.9	13.1		

To estimate relative sensitivities between the other beams and the reference beam, reflectivity factors are estimated at all profiles and range gates using equation (8) with $C_{relative}^{OtherMode}$ set to zero, and then estimating the differences from nearby precipitation short-pulse mode observations. Figure 10 shows scatter plots and histograms of reflectivity factor differences for the precipitation long-pulse beam during the 7-June-2018 rain event. Valid observations are constrained to be within the range of 800 and 2100 m and precipitation short-pulse reflectivity factors greater than 30 dBZ. Over 13,000 valid samples are used from this event to calibrate the precipitation long-pulse beam. The mean relative offset is 15.5 dB for this event, with a standard deviation of 1.3 dB. The relative calibration constant $C_{relative}^{PrecipLong}$ is set to 15.5 dB and implies that the long-

https://doi.org/10.5194/egusphere-2022-1405
Preprint. Discussion started: 10 January 2023

pulse mode is more sensitive and produces a larger signal-to-noise ratio for the same radar reflectivity factor as expressed in equation (8).

Figure 11a and 11b show the time-height cross-sections of cross-calibrated precipitation short- and long-pulse reflectivity factors at their native resolution for the 7-June-2018 rain event. Figure 11c shows the precipitation long-pulse relative calibration offset for each matched short- and long-pulse observation. The relative calibration offsets shown in Fig. 11c are the same samples used to produce Fig. 10 and indicate the limited height range used in the comparison to avoid large reflectivity gradients near the radar bright band due to melting particles. Calibrating the three wind beams follows the same procedure used for calibrating the precipitation long-pulse beam (results are not shown due to space limitations).

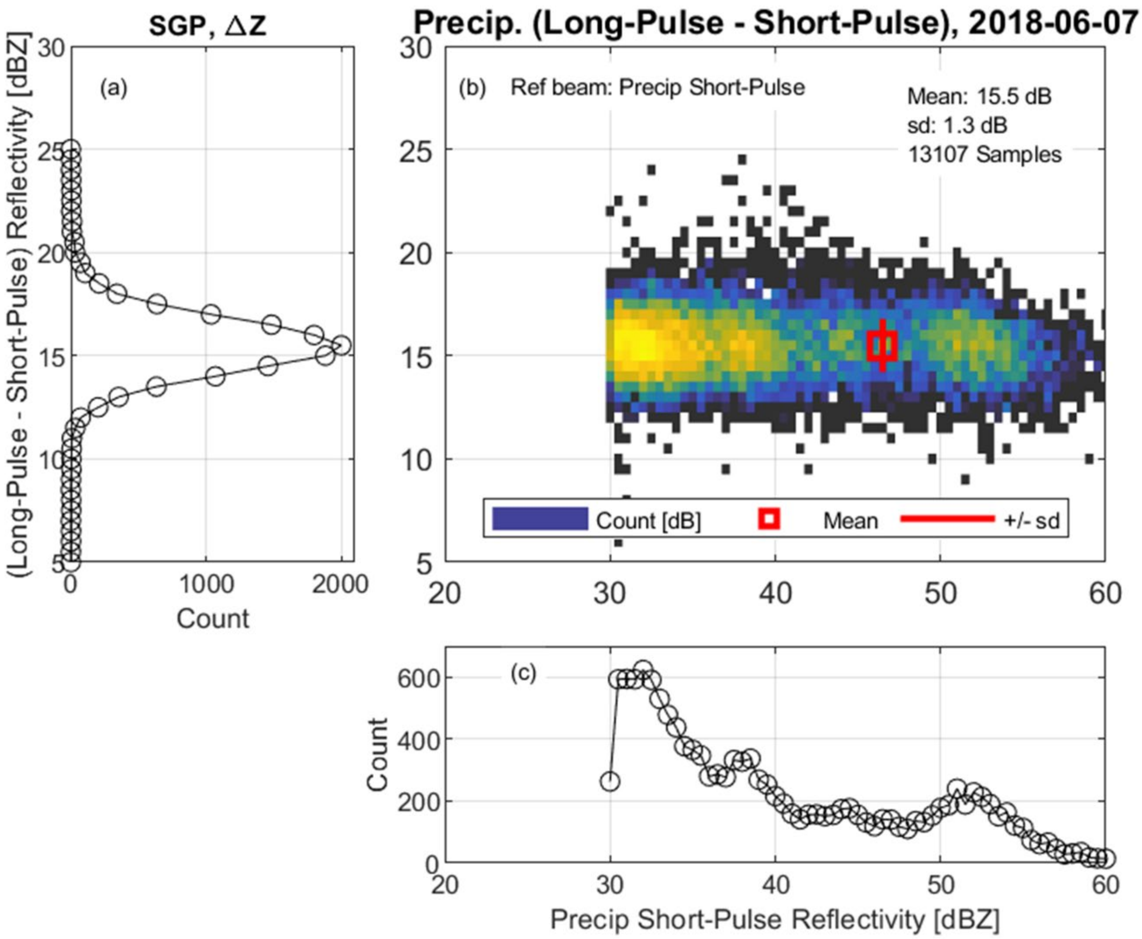

Figure 10. Reflectivity factor differences between precipitation long-pulse beam with $C_{relative}^{PrecipLong} = 0$ [dB] and disdrometer calibrated precipitation short-pulse beam observations for the rain event on 7-June-2018. Observations are limited to height ranges between 800 and 2100 m and precipitation short-pulse beam reflectivity greater than 30 dBZ. (a) Histogram of reflectivity difference (long-pulse – short-pulse) and indicates relative calibration offset, (b) relative 2-dimensional count of reflectivity difference, (c) histogram of disdrometer calibrated precipitation short-pulse reflectivity.

https://doi.org/10.5194/egusphere-2022-1405
Preprint. Discussion started: 10 January 2023

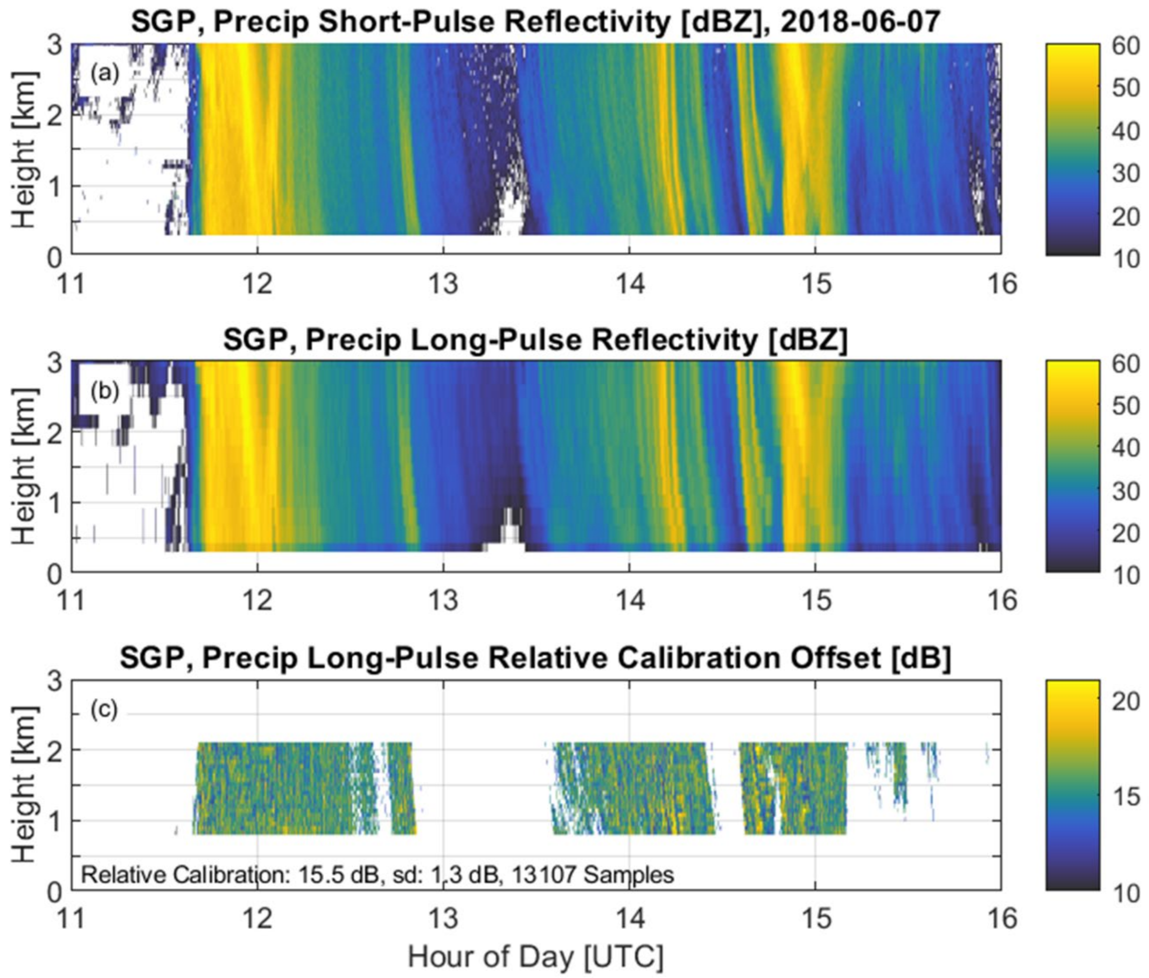

Figure 11. Time-height cross-sections for the 7-June-2018 rain event. (a) Surface disdrometer calibrated precipitation short-pulse reflectivity factor $Z^{PrecipShort}$, (b) cross-calibrated precipitation long-pulse reflectivity factor $Z^{PrecipLong}$ with $C^{PrecipLong}_{relative}$ = 15.5 dB, and (c) the precipitation long-pulse relative calibration offset for each matched short- and long-pulse observation. Relative calibration offset is only calculated for $Z^{PrecipShort} > 30$ dBZ and for ranges 800 and 2100 m.

4 Results

This section explores how the individual rain event precipitation short-pulse beam calibration constants varied over the 8-year record from 22-March-2011 to 18-August-2019. The variation of the relative calibration constants is examined as a function of ageing hardware and a function of changing radar hardware after equipment failures.

4.1 Reference Beam Calibration: Event, Monthly, and 3-Month Intervals

From 22-March-2011 to 18-August-2019, the precipitation short-pulse beam calibration constant $C^{PrecipShort}$ was estimated on 340 days, each having at least 120 minutes of surface disdrometer reflectivity factor greater than 20 dBZ. Figure 12

https://doi.org/10.5194/egusphere-2022-1405
Preprint. Discussion started: 10 January 2023

shows $C^{PrecipShort}$ for every valid precipitation event using black plus symbols. The calibration constant is approximately -50 dB at the beginning of this record in 2011 and then increases to about -35 dB near the beginning of 2015. There is an abrupt drop in calibration constant near the end of 2015, and then the calibration constant steadily increases until the end of this dataset in 2019. Snow events were not included in the calibration procedure.

An increase in calibration constant, without changing operating parameters, indicates the radar sensitivity is degrading. Referring to equation (6), if the reflectivity factor is constant and the measured SNR decreases because of ageing radar hardware, then the calibration constant must increase. Thus, from early 2012 to mid-2015, the approximate 15 dB increase in calibration constant indicates approximately 4 dB/year decrease in radar sensitivity. Though not documented publicly, similar decreasing sensitivity rates have been estimated in other NOAA UHF wind profilers and have been attributed to delamination of the fibreglass patch antenna (Ecklund et al., 1988).

The gaps in measurements in mid-2015 and early 2017 are when the radar was not operating. New radar hardware was installed in September 2015, and the calibration constant dropped by about 10 dB relative to the old hardware. In mid-2017, radar hardware was updated and the mean noise level dropped by about 7 dB (see Fig. 5), but the short-pulse beam calibration constant did not change significantly. The steady increase in calibration constant from 2016 through 2019 suggests an approximate 3 dB/year decrease in sensitivity for this modified radar.

The slow change in calibration constant between precipitation events suggests that the disdrometer-to-RWP calibration procedure could be performed using fixed time intervals instead of individual rain events. To test this hypothesis, calibration constants were determined using all rain events during 1-month and 3-month intervals (i.e., months of JFM, AMJ, JAS, and OND). The 1- and 3-month calibration constants are plotted in Fig. 12 using blue squares and red triangles, respectively. The blue and red vertical lines represent 1- and 3-month calibration constant standard deviations, with mean standard deviations over the 9-year record equal to 3.6 and 2.9 dB, respectively. These standard deviations represent variations due to spatiotemporal mismatch of surface disdrometer and radar measurements, instantaneous measurement uncertainties of both instruments, as well as aging hardware over the sampling interval.

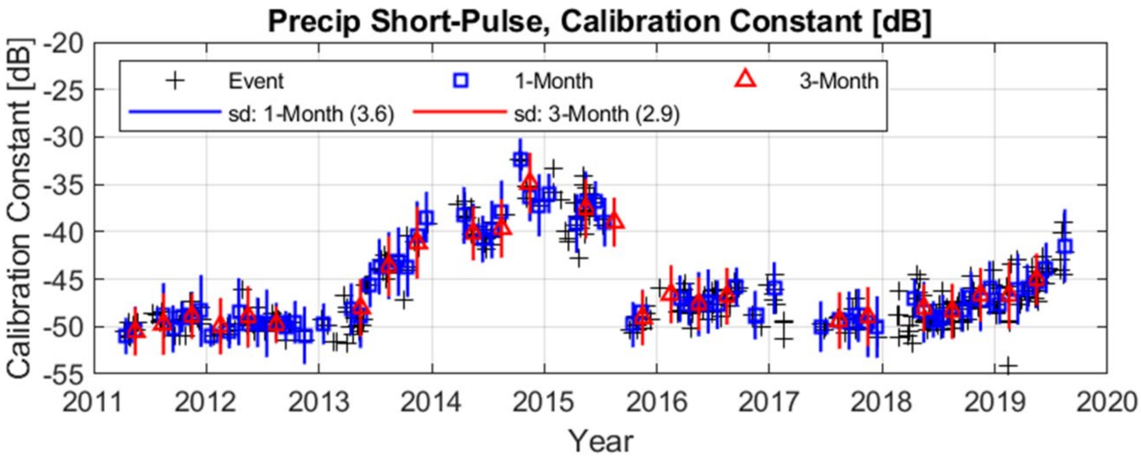

Figure 12. Precipitation short-pulse beam calibration constant $C^{PrecipShort}$ [dB] from March 2011 through July 2019 estimated using individual rain events (black plusses), 1-month interval (blue squares), and 3-month interval (red triangles). Vertical blue and red lines are +/- standard deviation for 1- and 3-month interval calculations, respectively. Mean standard deviations over the 9-year dataset were 3.6 and 3.0 dB for the 1- and 3-month intervals, respectively.

4.2 Relative Calibration for each Hardware Calibration Period

Since the radar operating parameters did not change during the 2011 to 2019 interval, variations in relative calibration constants will depend on changes to the radar hardware. This section examines how the precipitation long-pulse and wind mode relative calibration constants evolved with hardware changes.

4.2.1 Changes in Precipitation Long-Pulse Relative Calibration Constant

The relative calibration constants for the precipitation long-pulse beam were estimated for every day with at least 1000 precipitation short- and long-pulse range gate samples between 800 and 2100 m range and with precipitation short-pulse reflectivity factor greater than 30 dBZ. The lower height limit of 800 m is to ensure the long-pulse beam observations are beyond the radar blind zone, and the 2100 m limit is to avoid reflectivity factor gradients near the melting layer. The precipitation long-pulse relative calibration constant was estimated for the 690 days meeting these criteria and are shown in Fig. 13 using black crosses. The dashed lines are the mean relative calibration values for each stable hardware interval labelled A through E (see Table 2). The relative calibration constant mean and standard deviation for each interval are listed in Table 4.

https://doi.org/10.5194/egusphere-2022-1405
Preprint. Discussion started: 10 January 2023

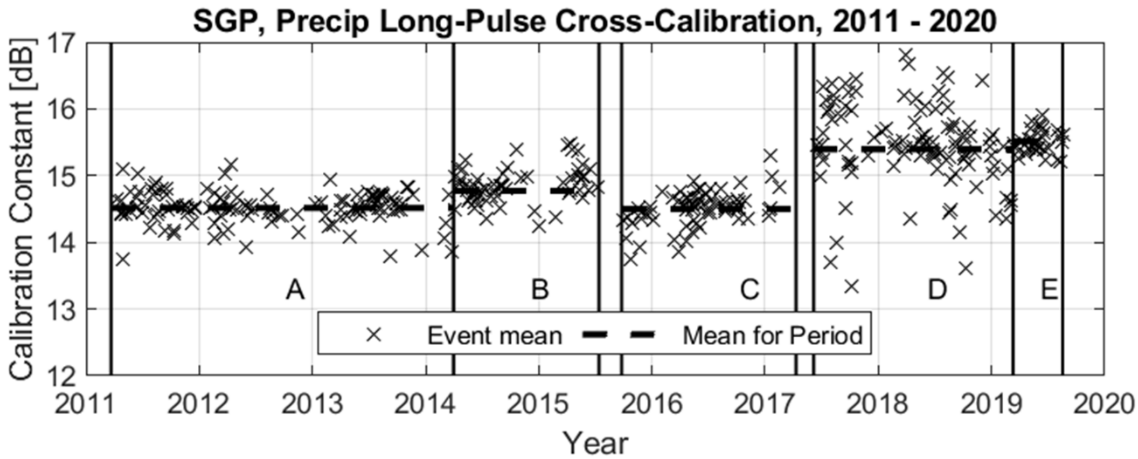

Figure 13. Precipitation long-pulse beam relative calibration constant $C^{PrecipLong}$ [dB] from 22-March-2011 through 18-August-2019 estimated using individual rain events (black crosses). Thick dashed lines are mean relative calibration constants (listed in Table 4) for stable hardware intervals labelled A through E as described in Table 2.

Table 4. RWP relative calibration constants [dB] (standard deviation) relative to precipitation short-pulse mode

			Precipitation		Wind Mode	
Period	Start	End	Long-Pulse	BeamV	BeamA	BeamB
A	22-March-2011	31-March-2014	14.5 (0.3)			
B	1-April-2014	14-July-2015	14.8 (0.3)	9.3 (0.7)	12.9 (3.1)	19.9 (2.3)
C	25-Sept-2015	10-April-2017	14.5 (0.3)	8.7 (0.7)	7.8 (1.1)	6.5 (1.5)
D	6-June-2017	10-March-2019	15.4 (0.7)	9.0 (0.9)	8.1 (2.6)	2.1 (2.9)
E	11-March-2019	18-August-2019	15.5 (0.2)			

4.2.2 Changes in Wind Mode Relative Calibration Constants

Similar to the conditions applied when estimating the precipitation long-pulse beam relative calibration constants, the wind mode beams were estimated for every day with at least 1000 range gate samples between 500 and 2100 m range and with precipitation short-pulse reflectivity factor greater than 30 dBZ. The wind mode has a shorter pulse length than the precipitation long-pulse beam, which enables valid wind observations down to 500 m. Figure 14 shows the daily relative calibration constants for the three wind beams (black crosses) with thick dashed lines representing the mean relative calibration constant for each hardware interval. The vertical beam relative calibration constant is fairly stable over the 2014 to 2019 observation period, with values listed in Table 4. There is more event-to-event variability in the oblique beam relative calibration constants compared to the vertical beam because there is more horizontal distance between the vertical

https://doi.org/10.5194/egusphere-2022-1405
Preprint. Discussion started: 10 January 2023

pointing reference beam and the oblique beams. A 14° off-vertical pointing angle causes approximately 250 m horizontal distance between the vertical beam and oblique beam at 1 km height. Aside from the larger event-to-event variability, the oblique beam mean relative calibration constants change for each radar hardware configuration. This is probably due to changes in the antenna phase shift module that controls the antenna beam pattern and pointing direction. Table 4 lists the mean oblique beam relative calibration constants for each hardware configuration.

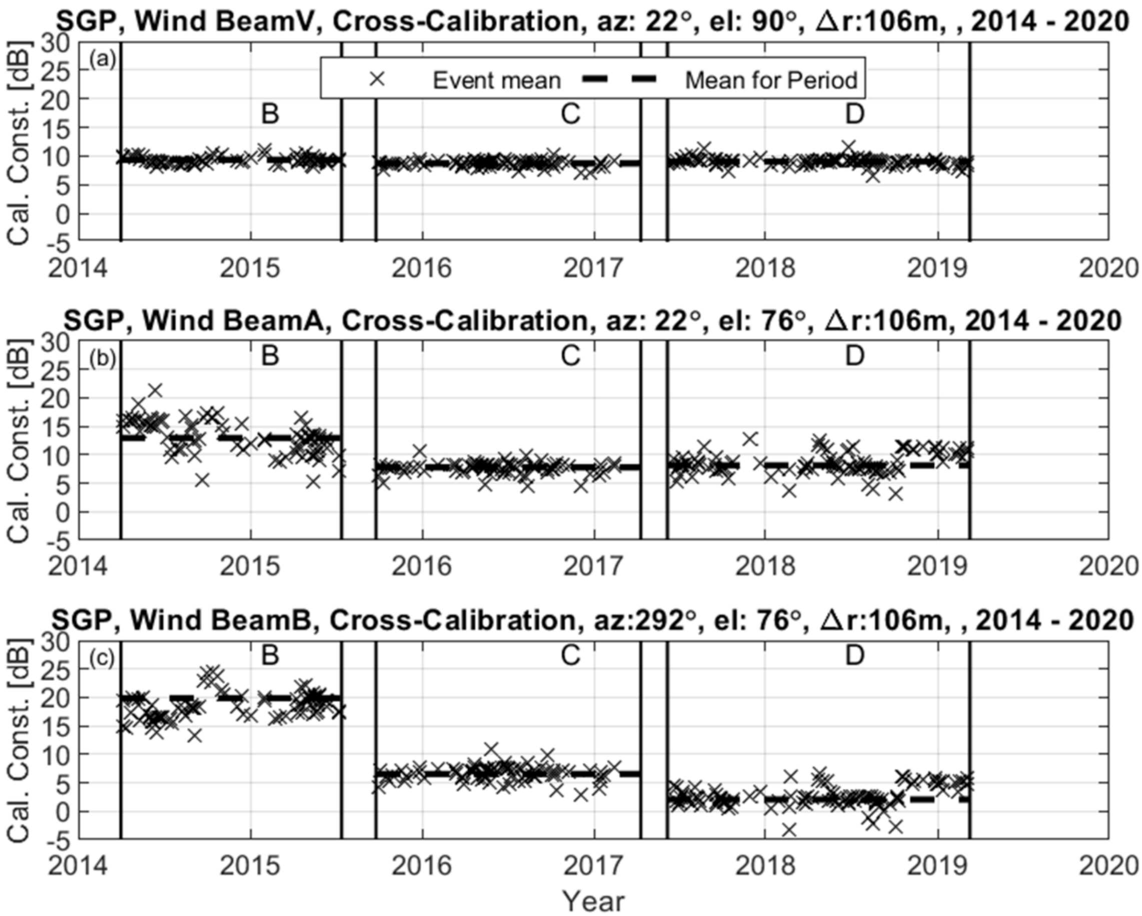

Figure 14. Relative calibration constants for wind mode for every rain event from March 2014 through February 2019. (a) Vertical beam (beamV, az: 22°, el: 90°), (b) oblique beam (beamA, az: 22°, el: 76°), and (c) oblique beam (beamB, az: 292°, el: 76°). Thick dashed lines are mean relative calibration constants (listed in Table 4) for stable hardware intervals labelled B, C, and D as described in Table 2.

5 Conclusions

This work describes a procedure to calibrate a UHF band radar wind profiler (RWP) reflectivity factor to surface disdrometer observations. The revised procedure builds on the method described in Tridon et al. (2013) by correcting the recorded Doppler velocity power spectra due to Nyquist velocity aliasing and coherent integration bias effects before recalculating the

https://doi.org/10.5194/egusphere-2022-1405
Preprint. Discussion started: 10 January 2023

spectrum moments. The revised method also calibrates the oblique pointing RWP beams that are used to measure horizontal wind motions.

This cross-calibration procedure uses precipitation measurements from one instrument (i.e., surface disdrometer) as the reference dataset and then calibrates another instrument (i.e., the RWP) using measurements from the same precipitation event. This method cannot identify any biases in measurements from either instrument and the difference in measurements also includes instrument measurement uncertainties. To address biases, the calibration procedure is structured so that a single calibration constant establishes the disdrometer-to-radar calibration. Then, if future comparisons with another instrument determine the disdrometer-to-radar calibration is biased, a simple offset can be added to the radar reflectivity factor.

Regarding measurement uncertainties, the standard deviation of the reflectivity factor difference (i.e., $sd[Z^{PrecipShort} - Z^{Disdrometer}]$) includes variability due to different measurement technologies and due to spatiotemporal differences between measurements made at the surface and 500 m above the ground. The radar-to-disdrometer reflectivity factor difference standard deviations were similar in magnitude (i.e., approximately 2 dB) to standard deviations from side-by-side surface disdrometers measuring the same precipitation event (Tapiador et al., 2017; Wang et al., 2021). Thus, the reflectivity factor difference standard deviation is a relative measure indicating the quality of the comparison and is larger than a calibration constant uncertainty.

The calibration procedure determined an absolute calibration constant for the precipitation short-pulse beam, which was then called the “reference” beam. The relative calibration between this reference beam and all other beams was determined enabling all beams to be cross-calibrated to the surface disdrometer, including the RWP oblique pointing beams. The horizontal distance between the vertically pointing reference and oblique pointing beams caused an increase in event-to-event variability in the oblique beam relative calibration constant, as the two radar beams were observing different regions of the same precipitation event.

The precipitation short-pulse calibration constant changed over the 8-year dataset. The calibration constant tended to increase over time, corresponding to a decrease in radar sensitivity, consistent with hardware degrading over time. Referencing equation (6), degrading hardware will produce smaller SNR for the same radar reflectivity factor, which is compensated with a larger calibration constant. The radar sensitivity increased significantly (i.e., over 10 dB) when degraded hardware was replaced with new hardware. Between 2016 and 2019, the RWP radar reduced sensitivity at a rate of about 3-to-4 dB/year. The slow change in radar sensitivity implies that the calibration constant can be computed using many rain events over a 1- or 3-month interval.

To promote the calibration of radar wind profilers and other radar systems, the processing codes used in this study are available on a public GitHub repository (Williams, 2022). This code is being incorporated into the ARM RWP processing suite with the intent of ARM RWP spectra being reprocessed using this calibration procedure. Also, the 8-years of data processed in this study are available on the ARM Archive as a PI product (Williams, 2023).

https://doi.org/10.5194/egusphere-2022-1405
Preprint. Discussion started: 10 January 2023

Code availability. The Python code that processes the raw Doppler velocity power spectra is available on GitHub (https://github.com/ChristopherRWilliams/RWP_Python_Moments).

Data availability. All raw observations used in this study are available on-line using the DOE ARM data discovery tool: http://dx.doi.org/10.5439/1025128, http://dx.doi.org/10.5439/1025129, http://dx.doi.org/10.5439/1025136, http://dx.doi.org/10.5439/1025137, and http://dx.doi.org/10.5439/1025315.

During the review process, the calibrated RWP moments are available in a DropBox folder (https://www.dropbox.com/sh/d83nvdwg9ouqtz3/AAD-WlKzDQ6ZePfrcSChm3hta?dl=0). A request has been submitted for DOE ARM to host these data as a PI Product for permanent storage. After DOE has approved this request, the DropBox link will be disabled and this manuscript text will be:

The calibrated RWP moments produced in this study are available on the DOE ARM archive a PI Product at this link: https://iop.archive.arm.gov/arm-iop/0pi-data/williams/TBD.

Author contribution. CRW, PM, and SG conceptualized the study. CRW developed the spectral processing software in the MATLAB language and performed the analysis. JB converted the MATLAB code into Python code. PEJ developed the coherent integration and SNR adjustment methodologies. CRW wrote the manuscript and all authors reviewed and edited the manuscript.

Competing interests. The authors declare that they do not have any competing interests.

Disclaimer. Authors do not state any disclaimers.

Acknowledgments. This research received funding through the DOE Atmospheric System Research (ASR) program under award DE-SC0021345. Additionally, PEJ was supported by NOAA Physical Sciences Laboratory and CIRES through the NOAA cooperative agreement NA17OAR4320101. We recognize and appreciate the work of field technicians deployed year-round to Southern Great Plains and tasked with keeping these instruments running. This research was supported by the Office of Biological and Environmental Research of the US Department of Energy as part of the Atmospheric Radiation Measurement (ARM) Climate Research Facility, and Office of Science scientific user facility.

https://doi.org/10.5194/egusphere-2022-1405
Preprint. Discussion started: 10 January 2023

References

Angevine, W. M., Buhr, M. P., Holloway, J. S., Trainer, M., Parrish, D. D., MacPherson, J. I., Kok, G. L., Schillawski, R. D., and Bowlby, D. H.: Local meteorological features affecting chemical measurements at a North Atlantic coastal site, J. Geophys. Res., 101, 28935-28945, 1996.

Angevine, W. M., Grimsdell, A. W., McKeen, S. A., and Warnock, J. M.: Entrainment results from the Flatland boundary layer experiments, J. Geophys. Res., 103, 13689-13701, 1998.

Atmospheric Radiation Measurement (ARM) user facility: Radar Wind Profiler (915RWPPRECIPMOM). 2011-03-22 to 2019-08-18, Southern Great Plains (SGP) Central Facility, Lamont, OK (C1). Compiled by P. Muradyan. ARM Data Center. Data set accessed: 01 August 2021, http://dx.doi.org/10.5439/1025128, 1998a.

Atmospheric Radiation Measurement (ARM) user facility: Radar Wind Profiler (915RWPPRECIPSPEC). 2011-03-22 to 2019-08-18, Southern Great Plains (SGP) Central Facility, Lamont, OK (C1). Compiled by P. Muradyan. ARM Data Center. Data set accessed: 10 October 2022, at http://dx.doi.org/10.5439/1025129, 1998b.

Atmospheric Radiation Measurement (ARM) user facility: Radar Wind Profiler (915RWPWINDMOM). 2014-03-06 to 2019-03-10, Southern Great Plains (SGP) Central Facility, Lamont, OK (C1). Compiled by P. Muradyan. ARM Data Center. Data set accessed: 01 August 2021, http://dx.doi.org/10.5439/1025136, 1998c.

Atmospheric Radiation Measurement (ARM) user facility: Radar Wind Profiler (915RWPWINDSPEC). 2014-03-06 to 2019-03-10, Southern Great Plains (SGP) Central Facility, Lamont, OK (C1). Compiled by P. Muradyan. ARM Data Center. Data set accessed: 01 August 2021, http://dx.doi.org/10.5439/1025137, 1998d.

Atmospheric Radiation Measurement (ARM) user facility: Video Disdrometer (VDIS). 2011-03-22 to 2019-08-18, Southern Great Plains (SGP) Central Facility, Lamont, OK (C1). Compiled by D. Wang. ARM Data Center. Data set accessed: 01 August 2021, http://dx.doi.org/10.5439/1025315, 2011.

Atmospheric Radiation Measurement (ARM) user facility: Formatting and file naming protocols, downloaded 31 August 2022, https://www.arm.gov/policies/datapolicies/formatting-and-file-naming-protocols, 2022.

Carter, D. A., Gage, K. S., Ecklund, W. L., Angevine, W. M., Johnston, P. E., Riddle, A. C., Wilson, J. S., and Williams,C. R.: Developments in UHF lower tropospheric wind profiling at NOAA's Aeronomy Laboratory, Radio Science, 30, 977-1001, 1995.

https://doi.org/10.5194/egusphere-2022-1405
Preprint. Discussion started: 10 January 2023

Chandrasekar, V., Baldini, L., Bharadwaj N., and Smith,P. L.: Calibration procedures for global precipitation-measurement ground-validation radars, URSI Radio Science Bulletin, 355, 45-73, https://doi.org/10.23919/URSIRSB.2015.7909473, 2015.

Ecklund, W. L., Carter, D. A., and Balsley, B. B.: A UHF wind profiler for the boundary layer: Brief description and initial results, J. Atmos. Oceanic Technol., 5, 432–441, https://doi.org/10.1175/1520-0426(1988)005<0432:AUWPFT>2.0.CO;2, 1988.

Farley, D. T.: On-line data processing techniques for MST radars, Radio Sci., 20, 1177-1184, 1985.

Gage, K. S. and Balsley, B. B.: Doppler radar probling of the clear atmosphere, Bull. Amer. Meteor. Soc., 59, 1074-1093, 1978.

Gage, K. S., Williams, C. R., and Ecklund, W. L.: UHF wind profilers: A new tool for diagnosing tropical convective cloud systems, Bull. Amer. Meteorol. Soc.,75, 2289-2294, 1994.

Gage, K. S., Williams, C. R., Johnston, P. E., Ecklund, W. L., Cifelli, R., Tokay, A. and Carter, D. A.: Doppler radar profilers as calibration tools for scanning radars, J. Appl. Meteor., 39, 2209–2222, 2000.

Giangrande, S. E., Wang, D., Bartholomew, M. J., Jensen, M. P., Mechem, D. B., Hardin, J. C., and Wood, R.: Midlatitude oceanic cloud and precipitation properties as sampled by the ARM Eastern North Atlantic Observatory. J. Geophys. Res: Atmos, 124, 4741– 4760. https://doi.org/10.1029/2018JD029667, 2019.

Hardin, J., and Guy, N.: PyDisdrometer (PyDSD), http://doi.org/10.5281/zenodo.9991, 2014.

Hartten, L. M., Johnston, P. E., Castro, V. M. R., and Pérez, P. S. E.: Postdeployment calibration of a tropical UHF profiling radar via surface- and satellite-based methods, J. Atmos. Oceanic Technol., 36, 1729–1751, https:// doi.org/10.1175/JTECH-D-18-0020.1, 2019.

Hildebrand, P. H., and Sekhon, R. S.: Objective determination of the noise level in Doppler spectra, J. Appl. Meteor., 13, 808-811, 1974.

Kollias, P., Treserras, B. P., and Protat, A.: Calibration of the 2007–2017 record of Atmospheric Radiation Measurements cloud radar observations using CloudSat, Atmos. Meas. Tech., 12, 4949–4964, doi:10.5194/amt-12- 4949-2019, 2019.

Mather, J. H. and Voyles, J. W., : The ARM climate research facility: A review of structure and capabilities, Bull. Amer. Meteorol. Soc., 94, 377–392, 2013.

Merritt, D. A.: A Statistical Averaging Method for Wind Profiler Doppler Spectra, J. Atmos. Ocean. Tech., 12, 985–995, https://doi.org/10.1175/15200426(1995)012<0985:ASAMFW>2.0.CO;2, 1995.

Muradyan, P, and Coulter, R.: Radar Wind Profiler (RWP) and Radio Acoustic Sounding System (RASS) instrument handbook, U. S. Department of Energy, Atmospheric Radiation Measurement user facility, DOE/SC-ARM-TR-044, https://doi.org/10.2172/1020560, 2020.

National Oceanic and Atmospheric Administration (NOAA): Physical System Laboratory Wind Profiler Network Data and Image Library, accessed on: 17 October 2022, https://psl.noaa.gov/data/obs/datadisplay/, 2022.

Protat, A., Bouniol, D., O'Connor, E. J., Baltink, H. K., Verlinde, J., and Widener, K.: CloudSat as a global radar calibrator, J. Atmos. Oceanic Technol., 28, 445-452, https://doi.org/10.1175/2010JTECHA1443.1, 2011.

Protat, A., Louf, V., Soderholm, J., Brook, J., and Ponsonby, W.: Three-way calibration checks using ground-based, ship-based, and spaceborne radars, Atmos. Meas. Tech., 15, 915-926, https://doi.org/10.5194/amt-15-915-2022, 2022.

Riddle, A. C., Hartten, L. M., Carter, D. A., Johnston, P. E., and Williams, C. R.: A minimum threshold for wind profiler signal-to-noise ratios, J. Atmos Oceanic Technol., 29, 889-895, https://doi.org/10.1175/JTECH-D-11-00173.1, 2012.

Rogers, R. R., Ecklund, W. L., Carter, D. A., Gage, K. S., and Ethier, S. A. : Research applications of a boundary-layer wind profiler, Bull. Amer. Meteor. Soc., 74, 567-580, https://doi.org/10.1175/1520-0477(1993)074<0567:RAOABL>2.0.CO;2, 1993.

Schmidt, G., Rüster, R., Czechowsky, P.: Complementary codes and digital filtering for detection of weak VHF radar signals from the mesosphere, IEEE Trans. Geosci.Electron., GE-17, 154-161, 1979.

Schönhuber, M., Lammer, G., and Randeu, W. L.: The 2D-Video-Disdrometer, in: Precipitation: Advances in Measurement, Estimation and Prediction, Springer, Heidelberg, Germany, 3-31,https://doi.org/10.1007/978-3-540-77655-0_1, 2008.

Tapiador, F. J., Navarro, A., Moreno, R., Jiménez-Alcázar, A., Marcos, C., Tokay, A., Durán, L, Bodoque, J. M., Martín, R., Petersen, W., and de Castro, M., On the optimal measuring area for pointwise rainfall estimations: A dedicated experiment with 14 laser disdrometers, J. Hydro, 18, 753-760, https://doi.org/10.1175/JHM-D-16-0127.1, 2017.

Tokay, A., Kruger, A., and Krajewski, W. F.: Comparison of drop size distribution measurements by impact and optical disdrometers, J. App. Meteor. Climat., 40, 2083–2097, https://doi.org/10.1175/1520-0450(2001)040 <2083:CODSDM>2.0.CO;2, 2001.

https://doi.org/10.5194/egusphere-2022-1405
Preprint. Discussion started: 10 January 2023

Tokay, A., Petersen, W. A., Gatlin, P., and Wingo, M.: Comparison of raindrop size distribution measurements by collocated disdrometers, J. Atmos. Oceanic Technol., 30: 1672–1690, https://doi.org/10.1175/JTECH-D-12-00163.1, 2013.

Tridon, F., Battaglia, A., Kollias, P., Luke, E., and Williams, C. R.: Signal postprocessing and reflectivity calibration of the Atmospheric Radiation Measurement Program 915-MHz Wind Profilers, J. Atmos. Ocean. Tech., 30, 1038-1054. https://doi.org/10.1175/JTECH-D-12-00146.1, 2013.

Vaisala News, “Wind Profilers Added to Vaisala Product Range”, available on line, www.vaisala.com/sites/default/files/documents/VN158_Wind_Profilers_Added_to_Vaisala_Product_Range.pdf, accessed 17-August-2022.

Wang D., Bartholomew, M., Giangrande, S. E., and Hardin, J. C.: Analysis of three types of collocated disdrometer measurements at the ARM southern great plains observatory, U. S. Department of Energy, Atmospheric Radiation Measurement user facility, DOE/SC-ARM-TR-275, https://doi.org/10.2172/1828172, 2021.

Williams, C. R., Gage, K. S., Clark, W., and Kucera, P. : Monitoring the reflectivity calibration of a scanning radar using a profiling radar and a disdrometer, J. Atmos. Oceanic Technol., 22, 1004-1018, 2005.

Williams, C. R., Maahn, M., Hardin J. C., and de Boer, G., Clutter mitigation, multiple peaks, and high-order spectral moments in 35-GHz vertically pointing radar velocity spectra, J. Atmos. Meas. Tech., 11, 4963-4980, https://doi.org/10.5194/amt-11-4963-2018, 2018.

Williams, C. R.: Radar Wind Profiler (RWP) processing codes in Python, https://github.com/ChristopherRWilliams/rwp/Python/spectra, last accessed TBD (approximately 16-Dec-2022), 2022.

Williams, C. R.: Calibrated Radar Wind Profiler (RWP) moments from SGP, https://iop.archive.arm.gov/arm-iop/0pi-data/williams/rwp, last accessed TBD (approximately 15-Jan-2023), 2023.